2D MATERIALS

Wigner molecular crystals from multielectron moiré artificial atoms

Hongyuan Li[1,2,3]†*, Ziyu Xiang[1,2,3]†, Aidan P. Reddy[4], Trithep Devakul[4], Renee Sailus[5], Rounak Banerjee[5], Takashi Taniguchi[6], Kenji Watanabe[7], Sefaattin Tongay[5], Alex Zettl[1,3,8], Liang Fu[4]*, Michael F. Crommie[1,3,8]*, Feng Wang[1,3,8]*

Semiconductor moiré superlattices provide a versatile platform to engineer quantum solids composed of artificial atoms on moiré sites. Previous studies have mostly focused on the simplest correlated quantum solid—the Fermi-Hubbard model—in which intra-atom interactions are simplified to a single onsite repulsion energy *U*. Here we report the experimental observation of Wigner molecular crystals emerging from multielectron artificial atoms in twisted bilayer tungsten disulfide moiré superlattices. Using scanning tunneling microscopy, we demonstrate that Wigner molecules appear in multielectron artificial atoms when Coulomb interactions dominate. The array of Wigner molecules observed in a moiré superlattice comprises a crystalline phase of electrons: the Wigner molecular crystal, which is shown to be highly tunable through mechanical strain, moiré period, and carrier charge type.

Two-dimensional (2D) transition-metal dichalcogenide (TMDC) moiré superlattices provide a powerful platform to simulate strongly correlated quantum solids in which each moiré unit cell contains one or a few artificial atoms. Many new quantum phases, ranging from Mott insulators (*1*–*3*) and generalized Wigner crystals (*4*–*6*) to quantum anomalous Hall insulators (*7*–*11*), have been observed in different TMDC moiré superlattices. Most previous studies have focused on simulating the Fermi-Hubbard model in which intra-atom interactions are described by a single onsite repulsion energy U that neglects the intra-atom degrees of freedom. Recent theoretical studies (*12*–*14*), however, have predicted that multielectron artificial atoms in a moiré superlattice can host quantum states that exhibit unusual charge density distributions owing to a competition between the single-particle energy-level spacing Δ and the intra-atom Coulomb repulsion energy U (illustrated in Fig. 1A). Their ratio $\frac{U}{\Delta}$, usually defined as the Wigner parameter R_W (*15*, *16*), reflects the intra-atom interaction strength. At small R_W, the ground state of multielectron moiré atoms is well approximated by simply filling noninteracting orbitals in order of increasing energy. This results in a multielectron charge distribution that peaks at the center of the moiré potential well (Fig. 1B illustrates the three-electron case). At sufficiently large R_W, however, a qualitatively different electron configuration known as a Wigner molecule (*15*–*26*) is predicted to emerge, with electrons strongly localizing at different positions to minimize Coulomb energy (Fig. 1C illustrates the three-electron Wigner molecule regime). This interaction-dominated electronic structure involves substantial orbital reconstruction and is beyond the simplified Fermi-Hubbard model description. Although spectroscopic signatures of individual Wigner molecules have previously been observed in 2D electron gas–based quantum dots (*27*–*33*) and short carbon nanotubes (*34*, *35*), direct imaging of Wigner molecules has proved challenging. More notably, long-range ordering of Wigner molecules into Wigner molecular crystals (a distinct electronic crystalline phase) has not yet been seen. Here we develop a scanning tunneling microscopy (STM) imaging scheme to experimentally demonstrate the emergence of Wigner molecular crystals from multielectron artificial atoms in twisted WS_2 (tWS_2) moiré superlattices. Many-body simulations clarify the roles played by electron-electron interactions and the moiré potential in causing Wigner molecular crystal formation.

Experimental setup

Figure 1D illustrates our experimental setup and device configuration. A near-60° twisted tWS_2 bilayer is placed on top of a 49-nm-thick hexagonal boron nitride (hBN) layer and a graphite back gate. We use a graphene nanoribbon array as the electrical contact to reduce contact resistance to the tWS_2 layer (*36*, *37*). The carrier density of the tWS_2 is controlled by the bottom-gate voltage V_{BG}. A bias voltage V_{bias} is applied to the tWS_2 layer relative to the tip (which is grounded) for tunnel current measurement. Figure 1E shows a representative STM topographic image of the tWS_2 moiré superlattice, which exhibits a lattice constant of ~9 nm (corresponding to a twist angle of ~58°). Different high-symmetry stacking regions are labeled AB, $B^{S/S}$, and $B^{W/W}$, with the corresponding atomic structures illustrated in Fig. 1F. Previous studies have confirmed that the tWS_2 moiré superlattice creates deep moiré potential wells for electrons and holes that are localized at the $B^{W/W}$ (electrons) and AB (holes) stacking sites (*38*). This makes the tWS_2 moiré superlattice an ideal platform to explore multielectron artificial atoms and Wigner molecular crystals.

One of the main challenges for studying Wigner molecules in 2D semiconductors is the tip perturbation that occurs during tunneling measurements when a strong electrical field at the tip apex can qualitatively change local electron distributions. Previously we overcame this using a sensing layer–assisted STM technique that successfully imaged fragile TMD moiré correlated states (*4*, *39*). However, the sensing layer limits spatial resolution to ~5 nm, which is not sufficient to resolve the internal electron configuration of moiré artificial atoms. To overcome this difficulty, we have developed an STM scheme based on direct conduction–valence band edge tunnel current measurements.

Tunnel current measurement

Figure 2A illustrates our measurement scheme for electron-doped tWS_2 ($V_{BG} > 0$). Here the tip bias voltage V_{bias} is tuned to satisfy two conditions: (i) The chemical potential of the STM tip (μ_{tip}) must lie within the tWS_2 semiconductor bandgap and (ii) the vacuum energy levels of the tip and the tWS_2 must roughly align. When μ_{tip} is in the semiconductor bandgap, then the doped electrons in tWS_2 can tunnel into the STM tip and generate a finite current. Because this current comes from electrons near the conduction band edge, we denote it the CBE tunnel current. The CBE tunnel current directly reflects the electron spatial distribution in the tWS_2 layer. Because changing μ_{tip} over the entire bandgap does not alter the source of the CBE tunnel current, we can actively tune V_{bias} to roughly align the vacuum energy levels of the tip and tWS_2. Under these conditions, the electrical field between the tip and tWS_2 will be close to zero, thus minimizing the perturbation arising from the STM tip.

Figure 2B shows a 2D plot of the tunnel current *I*-*V* characteristic at the $B^{W/W}$ site as a function of V_{BG} and V_{bias} for electron-doped tWS_2 ($V_{BG} > 0$). Here the tunnel current is plotted on a logarithmic scale with different-color maps for positive current (yellow) and negative current (blue). The positions of the

[1]Department of Physics, University of California at Berkeley, Berkeley, CA, USA. [2]Graduate Group in Applied Science and Technology, University of California at Berkeley, Berkeley, CA, USA. [3]Materials Sciences Division, Lawrence Berkeley National Laboratory, Berkeley, CA, USA. [4]Department of Physics, Massachusetts Institute of Technology, Cambridge, MA, USA [5]School for Engineering of Matter, Transport and Energy, Arizona State University, Tempe, AZ, USA. [6]Research Center for Materials Nanoarchitectonics, National Institute for Materials Science, Tsukuba, Japan. [7]Research Center for Electronic and Optical Materials, National Institute for Materials Science, Tsukuba, Japan. [8]Kavli Energy NanoSciences Institute at the University of California Berkeley and the Lawrence Berkeley National Laboratory, Berkeley, CA, USA.
***Corresponding author. Email: hongyuan_li@berkeley.edu (H.L.); liangfu@mit.edu (L.F.); crommie@berkeley.edu (M.F.C.); fengwang76@berkeley.edu (F.W.)**
†These authors contributed equally to this work.

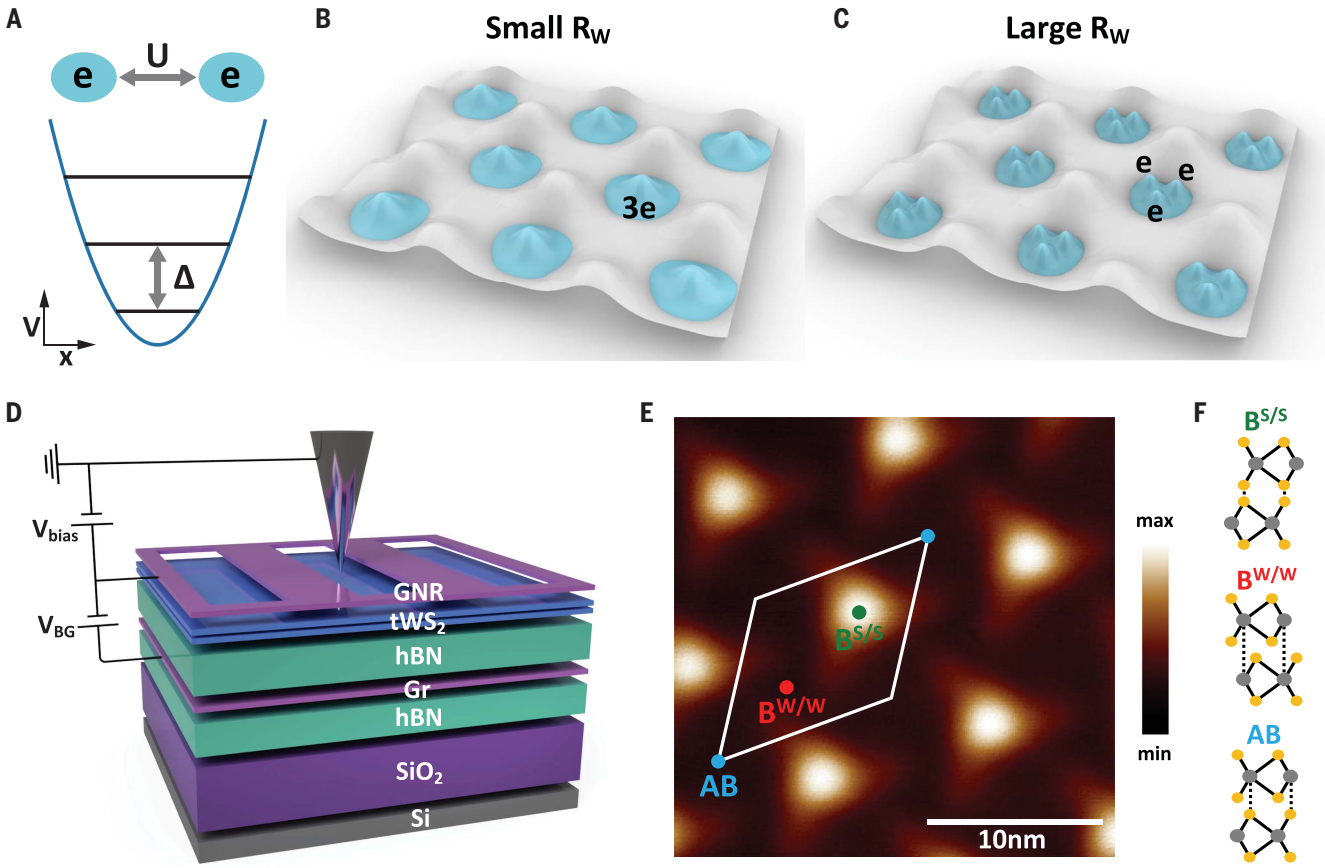

Fig. 1. Multielectron artificial atoms in a moiré superlattice. (**A**) Schematic of the intra-atom Coulomb repulsion energy U (top) and energy gap Δ between single-particle states in a parabolic potential well (bottom). The Wigner parameter R_W, defined as $\frac{U}{\Delta}$, reflects the internal interaction strength. (**B** and **C**) Illustration of an array of moiré artificial atoms with three electrons per moiré unit cell under different R_W values. (B) For small R_W, the three electrons in each artificial atom center around the potential minimum owing to the sixfold-degenerate single-particle ground states. (C) For large R_W, a triangular Wigner molecule charge configuration emerges in each artificial atom, generating a Wigner molecular crystal in the overall moiré superlattice. (**D**) Schematic of STM measurement setup for a gate-tunable near-58° tWS_2 moiré superlattice. tWS_2 is placed on top of a 49-nm-thick hBN layer and a graphite substrate that defines the back gate. A back-gate voltage V_{BG} is applied to control the charge carrier density in the tWS_2. A tip bias V_{bias} is applied between the tWS_2 and STM tip to induce a tunnel current. A graphene nanoribbon (GNR) array is placed on top of tWS_2 as the contact electrode. (**E**) A typical STM topographic image of the tWS_2 surface allows the identification of different high-symmetry stacking regions (AB, $B^{W/W}$, $B^{S/S}$). V_{bias} = −3V, I = 11 pA, V_{BG} = −5V. T = 5.4 K. (**F**) Atomic structure of the three different stacking regions in a moiré unit cell.

valence and conduction band edges are labeled with red and blue dashed lines, respectively [the method for identifying band edges for electron- (hole-) doped tWS_2 is shown in fig. S1 (S2)]. When μ_{tip} is in the semiconductor band gap ($-1.3V < V_{bias} < 0$), a small negative tunnel current is observed that corresponds to the CBE tunnel current illustrated in Fig. 2A. The V_{bias} dependence of the CBE tunnel current when μ_{tip} is in the energy gap region is characterized by a few steplike jumps. This arises from the Coulomb-induced tip perturbation, whereby charge accumulating at the tip apex can cause electrostatic charging or discharging of electrons in the artificial atom right below the tip. Experimentally we choose V_{bias} based on the criteria of minimizing the tip perturbation to best facilitate the imaging of Wigner molecules in artificial atoms [see materials and methods section 2 and fig. S3 for more details (*40*)].

The CBE tunnel current allows us to directly image the intra-atom electron distributions within each moiré unit cell. Figure 2, C to E, shows three CBE current maps for moiré artificial atoms with moiré site electron numbers of n_e = 1, 2, and 3 per artificial atom. At n_e = 1 (Fig. 2C, V_{bias} = −0.75 V, V_{BG} = 2.0 V), each moiré site exhibits a single peak centered at each $B^{W/W}$ site, corresponding to an electron strongly localized within the deep moiré potential. At n_e = 2 (Fig. 2D, V_{bias} = −0.75 V, V_{BG} = 4.0 V), the single peak remains but is broadened owing to strong intra-atomic repulsion that exceeds the single-particle gap, leading to considerable orbital spreading. This orbital spreading is a consequence of interaction-induced orbital mixing and cannot be captured by a one-band Fermi-Hubbard model in which interactions only alter the energetics but not the intra-atomic wave function. For n_e = 3 (Fig. 2E, V_{bias} = −0.75 V, V_{BG} = 6.0 V), we observe a qualitative change in the electron configuration: A trimer with three separated charge density peaks clearly emerges in each moiré artificial atom. Moreover, the electron density has a local minimum at the center of the artificial atom even though the moiré potential there is lowest. This is a direct visualization of a Wigner molecule, i.e., the electronic configuration in which intra-atom Coulomb repulsion U dominates over the single-particle quantized energy gap Δ, causing the multielectron ground state of the artificial atom to become fundamentally different from the picture of filling "atomic" shells. This also means that single-particle orbitals at low and

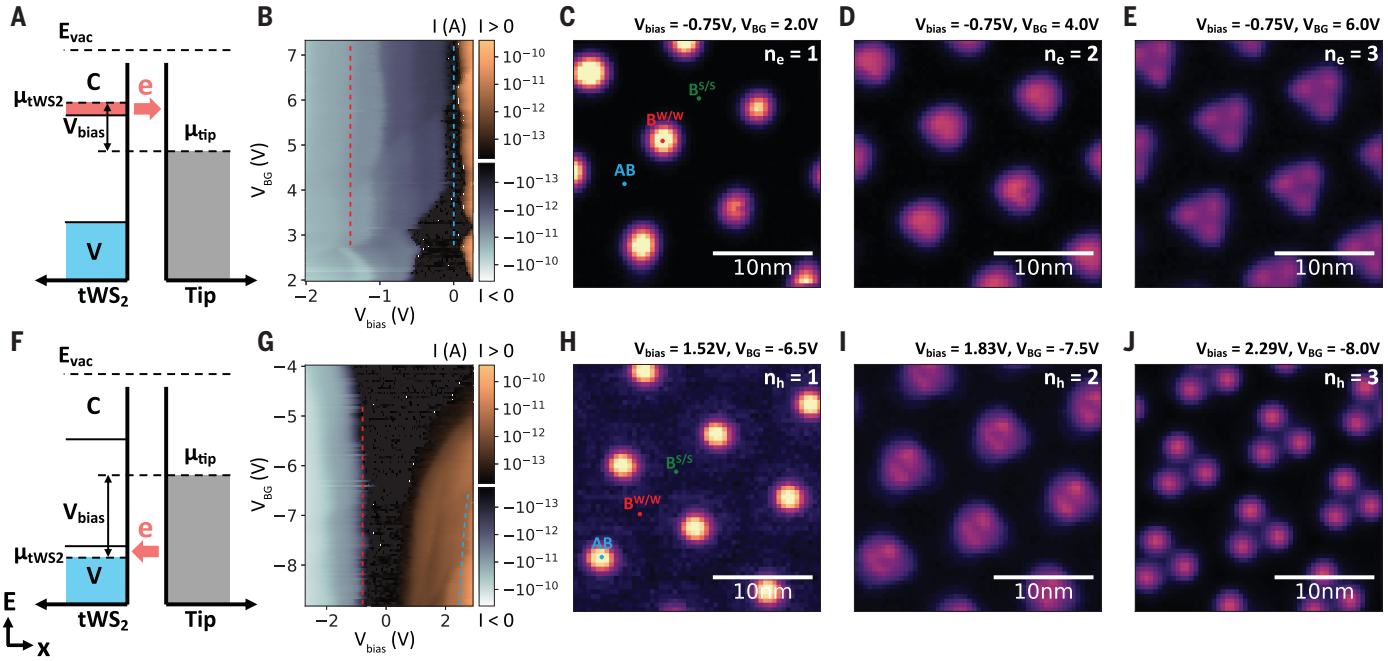

Fig. 2. CBE and VBE tunnel current measurement of Wigner molecules. (**A**) Schematic energy diagram for CBE tunnel current measurement of electron-doped tWS_2. The tWS_2 chemical potential μ_{tWS_2} is near the CBE. When the tip chemical potential μ_{tip} (controlled by V_{bias}) is aligned within the band gap of the tWS_2, the tunnel current arises from the doped electrons at the CBE. V_{bias} is tuned to roughly align the vacuum energy levels of the tip and tWS_2 so that the electric field near the tip apex is minimized. (**B**) Tunnel current *I-V* characteristic as a function of V_{BG} measured at the $B^{W/W}$ site for electron-doped tWS_2. The current is plotted on a logarithmic scale, and the positive (yellow) and negative (blue) parts use different-color maps. The valence and conduction band edges are labeled with red and blue dashed curves. (**C** to **E**). CBE tunnel current maps of artificial atoms with different electron numbers (n_e): (C) n_e = 1 (V_{bias} = −0.75 V, V_{BG} = 2.0 V), (D) n_e = 2 (V_{bias} = −0.75V, V_{BG} = 4.0 V), (E) n_e = 3 (V_{bias} = −0.75 V, V_{BG} = 6.0 V). (**F**). Schematic energy diagram for the VBE tunnel current measurement of hole-doped tWS_2. μ_{tWS_2} is near the VBE for hole-doped tWS_2. When μ_{tip} is aligned within the band gap of tWS_2, the tunnel current arises from doped holes at the VBE. The gap between μ_{tip} and μ_{tWS_2} is denoted as V^*_{bias} instead of V_{bias} because the real bias on the tunneling junction V^*_{bias} is lower than V_{bias} owing to the large contact resistance. (**G**). Tunnel current *I-V* characteristic as a function of V_{BG} measured at the AB site for hole-doped tWS_2 plotted similar to (B). Note that the VBE (labeled with the red dashed curve) is not located at V_{bias} = 0 owing to the large tip perturbation at negative V_{bias} [see additional details in (*40*)]. (**H** to **J**). VBE tunnel current maps of artificial atoms having different hole numbers (n_h): (H) n_h = 1 (V_{bias} = 1.52 V, V_{BG} = −6.5 V), (I) n_h = 2 (V_{bias} = 1.83 V, V_{BG} = −7.5 V), (J) n_h = 3 (V_{bias} = 2.29 V, V_{BG} = −8.0 V). T = 5.4 K for all the above measurements.

high energies are strongly mixed by Coulomb repulsion in multielectron moiré artificial atoms. The moiré site electron number n_e is identified through gate- and bias-dependent changes in the charge distribution current maps (see fig. S3 for additional details).

We can similarly measure the charge distributions of hole-doped artificial atoms using a valence band edge (VBE) current measurement scheme. Figure 2F illustrates the energy alignment diagram for STM measurement of hole-doped tWS_2 where μ_{tWS_2} now lies at the VBE and the VBE tunnel current is caused entirely by doped holes. The contact resistance is much larger for the hole-doped tWS_2 owing to a higher Schottky barrier, which leads to a non-negligible voltage drop at the electrical contact. As a result, we denote the electrical chemical potential difference between μ_{tip} and μ_{tWS_2} as V^*_{bias}, which can be smaller than the applied V_{bias} (*40*). Figure 2G shows a 2D plot of the tunnel current *I-V* characteristic at the AB site as a function of V_{BG} and V_{bias} for hole-doped tWS_2 (i.e., $V_{BG} < 0$). A nonzero VBE tunnel current is observed for 0.5 V < V_{bias} < 2.5 V when μ_{tip} is within the tWS_2 semiconductor bandgap. Figure 2, H to J, shows three VBE current maps for moiré artificial atoms with moiré site hole numbers of n_h = 1, 2, and 3. The n_h = 1 map (Fig. 2H) shows a single peak centered at the AB site, as expected for occupancy of a single hole. The n_h = 2 map (Fig. 2I), however, shows reduced charge density at the center of each moiré cell. Such a ring-like charge distribution is expected for a two-hole quantum Wigner molecule. The classical two-particle Coulomb molecule in a triangular potential well has threefold degeneracy (corresponding to three different orientations), and the quantum Wigner molecule is expected to be in a coherent superposition of all azimuthal configurations (with appropriate weights) (*14*, *15*), thus forming a ring-like pattern (see further discussion in "Modeling the Wigner molecular crystal" below). The asymmetry of the rings is caused by a slight uniaxial strain that breaks the C_3 rotational symmetry. The n_h = 3 map (Fig. 2J) shows a notable array of Wigner molecules wherein each has a clear trimer structure consisting of three well-isolated holes. The higher clarity for hole-based Wigner molecules (Fig. 2J) compared to electron-type Wigner molecules (Fig. 2E) suggests that the Wigner parameter $R_W = \frac{U}{\Delta}$ is larger for holes than for electrons in tWS_2, possibly because of a larger hole effective mass and shallower hole moiré potential.

Wigner molecular crystal geometry control

Other parameters that notably affect Wigner molecular crystal behavior are the moiré period and mechanical strain. Changing the moiré period alters the potential well width, thus modifying the correlation strength within a Wigner molecular crystal. Figure 3, A to C, shows the evolution of the three-electron Wigner molecule with decreasing moiré period λ [see definition of λ in (*40*) for lattices with nonzero strain]. As λ is reduced, the trimer

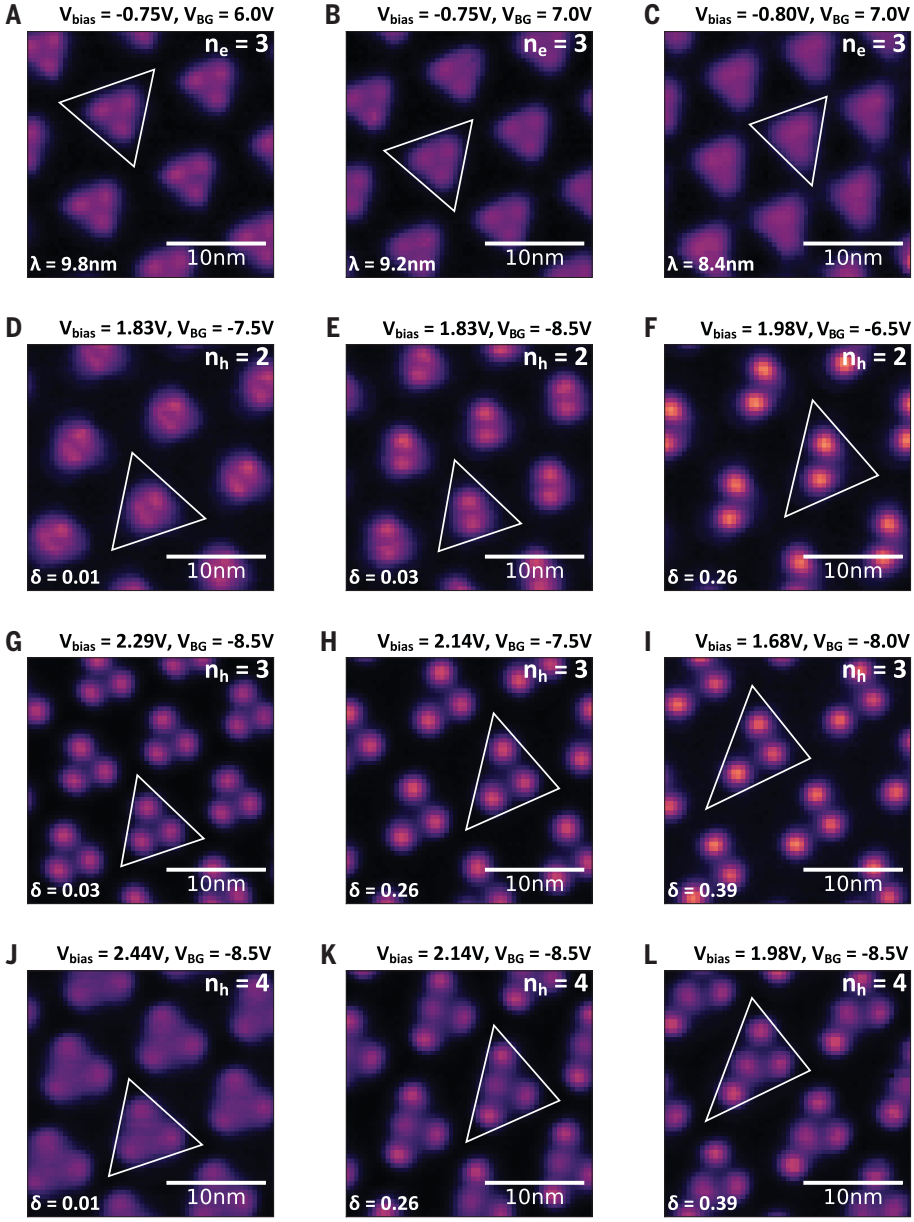

Fig. 3. Configuration engineering of Wigner molecular crystal. (**A** to **C**) Evolution of three-electron Wigner molecules as the moiré period is decreased from (A) $\lambda = 9.8$ nm to (B) $\lambda = 9.2$ nm, and to (C) $\lambda = 8.4$ nm. (**D** to **F**) Evolution of two-hole Wigner molecules as uniaxial strain is increased from (D) $\delta = 0.01$ to (E) $\delta = 0.03$, and to (F) $\delta = 0.26$. (**G** to **I**). Evolution of three-hole Wigner molecules as uniaxial strain is increased from (G) $\delta = 0.03$ to (H) $\delta = 0.26$, and to (I) $\delta = 0.39$. (**J** to **L**). Evolution of four-hole Wigner molecules as uniaxial strain is increased from (J) $\delta = 0.01$ to (K) $\delta = 0.26$, and to (L) $\delta = 0.39$. (A) and (D) are reproduced from Fig. 2, E and I, respectively. Exact definitions of λ and δ can be found in the supplementary materials (*40*). The white triangle in each panel labels the potential well contour. T = 5.4 K for all the above measurements.

features become gradually weaker, and the individual electrons are no longer distinguishable by $\lambda = 8.4$nm (Fig. 3C). This likely results from the reduction of the Wigner parameter R_W as the potential well becomes narrower with decreased λ, thus leading to a reduction in band mixing and more dominant single-particle behavior.

Uniaxial strain, by contrast, breaks the symmetry of the Wigner molecule spatial distribution. Figure 3, D to F, shows two-hole Wigner molecules as uniaxial strain is increased from $\delta = 0.01$ to $\delta = 0.26$ [see definition of δ in (*40*)]. The ring-like structure in Fig. 3D evolves into a well-defined dimer as strain is increased to $\delta = 0.26$ (Fig. 3F). Here strain breaks the C_3 symmetry of the moiré superlattice, thereby lifting the degeneracy of the three equivalent dimer directions and making one of them preferred as seen in Fig. 3, E and F. Figure 3, G to I, shows how uniaxial strain alters three-hole Wigner molecules and leads to elongated trimer structure with a modified internal particle distribution as strain is increased from $\delta = 0.03$ to 0.39. Figure 3, J to L, shows how uniaxial strain alters four-hole Wigner molecules as strain is increased from $\delta = 0.01$ to 0.39. The unusual pattern of four-hole Wigner molecules at low strain matches well with the recent theoretical prediction reported in (*14*). Similar strain-modified Wigner molecule behavior is also observed for electron-type Wigner molecules (see fig. S4 for more details).

Modeling the Wigner molecular crystal

The Wigner molecular crystals that we observe experimentally can be understood through a theoretical model that takes into account electron-electron interaction strength, moiré periodicity, and strain. Here we focus on the hole-doped regime in which the essential physics is captured by an effective continuum Hamiltonian for layer-hybridized Γ valley holes (*41*, *42*):

$$H = \sum_i \left\{ \frac{p_i^2}{2m} + \Delta(r_i) \right\} + \sum_{i<j} V_c(r_i - r_j)$$

Here $\Delta(r) = -2V_0 \sum_{n=1}^{3} \cos(g_n \cdot r + \phi)$ is the first-harmonic moiré potential with $g_n = \frac{4\pi}{\sqrt{3}\lambda}\left(\sin\frac{2\pi n}{3}, \cos\frac{2\pi n}{3}\right)$, $V_c(r) = \frac{e^2}{4\pi\epsilon r}$ is the interparticle Coulomb interaction potential, and m is the effective mass. The moiré potential has minima in the AB stacking regions and can be expanded thereabout as $\Delta(r) \approx \frac{1}{2}kr^2 + c_3 r^3 \cos(3\theta) + \ldots$ where $k = \frac{16\pi^2 V_0 \cos(\phi)}{\lambda^2}$ and $c_3 = \frac{16\pi^3 \sin(\phi)}{3^{3/2}\lambda^3}$, thus giving rise to effective "moiré atoms" with threefold anisotropy. The physics of the Wigner molecular crystal is controlled by three length scales (*12*): (i) the quantum confinement length $\xi_0 = \left(\frac{\hbar^2}{mk}\right)^{\frac{1}{4}}$, which determines the spread of the one-electron wave function; (ii) the Coulomb confinement length $\xi_c = \left(\frac{e^2}{16\pi\epsilon k}\right)^{\frac{1}{3}}$ which determines the equilibrium separation of two point-charges in a harmonic well; and (iii) the moiré period λ. The Wigner molecular crystal regime is characterized by a hierarchical relationship between these length scales: $\xi_0 < \xi_c < \lambda$.

We model the ground state charge density configuration of Wigner molecular crystals using two complementary approaches: self-consistent Hartree–Fock (HF) theory for the

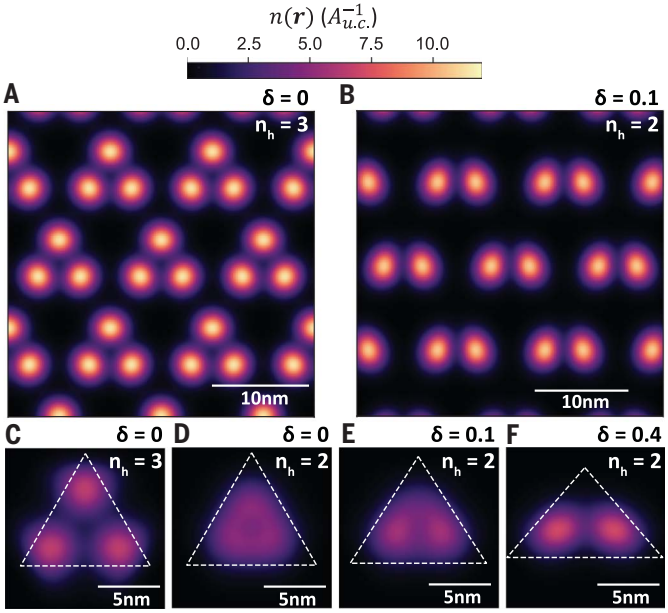

Fig. 4. Numerical simulations of Wigner molecular crystal. (**A**) Self-consistent Hartree–Fock (HF) ground-state hole density map for a continuum model with $n_h = 3$ (assuming full spin–valley polarization). (**B**) HF ground-state hole density map for $n_h = 2$ with S_z= 0 and applied strain [$\delta = 0.1$; see the supplementary materials (*40*) for definition]. (**C**) ED ground state for three fully spin-polarized electrons in a single moiré potential well. (**D** to **F**) ED ground state of two electrons in a singlet state with different values of strain: (D) $\delta = 0$, (E) $\delta = 0.1$, and (F) $\delta = 0.4$. The white dashed triangles in (C) to (F) label the potential well contour. $A_{u.c.}$ is the moiré unit cell area. The HF [(A) and (B)] and ED [(C) to (F)] results share the same color bar.

full continuum model, and exact diagonalization (ED) for single moiré atoms. HF accounts for the full moiré superlattice but treats electron interactions in mean-field, whereas ED treats electron correlations exactly but is restricted to a single artificial atom. The continuum model parameters that we have chosen correspond to a moiré atom energy-level spacing $\Delta \equiv \hbar\omega \approx 37meV$ (here $\omega = \sqrt{\frac{k}{m}}$ is the oscillator frequency) and intra-moiré-atom interaction energy $U \equiv \frac{e^2}{4\pi\epsilon\xi_o} \approx 190$ meV roughly consistent with previous works (*39*, *43*) and yielding $R_W \approx 5.1$ [see (*40*) for further details]. Figure 4A shows the resulting theoretical hole density obtained by HF for $n_h = 3$. The calculation yields a Wigner molecular crystal in good agreement with the experimental data of Fig. 2J. Figure 4B shows the HF hole density at $n_h = 2$ in the presence of a uniaxial strain of $\delta = 0.1$, which is seen to stabilize a dimer configuration that is consistent with the experimental data of Fig. 3F. However, we note that the HF results tend to spuriously break rotation symmetry of the two-hole molecules and yield a dimer even without strain [see further discussion in (*40*)]. This drawback does not occur in the ED calculations, which, however, are limited here to isolated single moiré atoms.

The ED charge density for a single unstrained moiré atom with three holes is seen in Fig. 4C and shows good overall agreement between the two numerical models and the experimental data. The unstrained $n_h = 2$ ED charge density of Fig. 4D, by contrast, shows a doughnut-like configuration that is more symmetrical than the data of Figs. 2I and 3D. After adding a small amount of strain to the ED calculation, however, the charge density relaxes in the strain direction and becomes more prolate (Fig. 4E), consistent with the experimental data of Figs. 2I and 3D. The $n_h = 2$ configuration is thus seen to be highly sensitive to strain while also exhibiting an inherently quantum delocalization effect arising from quantum fluctuations of the threefold-degenerate classical dimer configurations. A well-defined dimer configuration emerges in the ED charge density (Fig. 4F) with additional uniaxial strain that is similar to the experimental data of Fig. 3, E and F.

Conclusions and outlook

We observe the emergence of Wigner molecular crystals in moiré artificial atoms using an STM tunnel current measurement scheme. This state of matter represents an electron crystalline phase that arises from multielectron artificial atoms and has no analog in conventional quantum solids made from natural atoms. We show that Wigner molecular crystals can be manipulated by changing charge carrier type, moiré period, and mechanical strain in a moiré heterostructure. The intra-atom electron correlations within Wigner molecular crystals open up avenues to explore spin, charge, and topological phenomena that are distinct from conventional quantum solids.

REFERENCES AND NOTES

1. Y. Cao *et al.*, *Nature* **556**, 80–84 (2018).
2. G. Chen *et al.*, *Nat. Phys.* **15**, 237–241 (2019).
3. L. Wang *et al.*, *Nat. Mater.* **19**, 861–866 (2020).
4. H. Li *et al.*, *Nature* **597**, 650–654 (2021).
5. E. C. Regan *et al.*, *Nature* **579**, 359–363 (2020).
6. Y. Xu *et al.*, *Nature* **587**, 214–218 (2020).
7. T. Li *et al.*, *Nature* **600**, 641–646 (2021).
8. D. M. Kennes *et al.*, *Nat. Phys.* **17**, 155–163 (2021).
9. J. Cai *et al.*, *Nature* **622**, 63–68 (2023).
10. Y. Zeng *et al.*, *Nature* **622**, 69–73 (2023).
11. H. Park *et al.*, *Nature* **622**, 74–79 (2023).
12. A. P. Reddy, T. Devakul, L. Fu, *Phys. Rev. Lett.* **131**, 246501 (2023).
13. D. Luo, A. P. Reddy, T. Devakul, L. Fu, Artificial intelligence for artificial materials: moir\'e atom. *arXiv preprint arXiv:2303.08162*, (2023).
14. C. Yannouleas, U. Landman, *Phys. Rev. B* **108**, L121411 (2023).
15. C. Yannouleas, U. Landman, *Rep. Prog. Phys.* **70**, 2067–2148 (2007).
16. W. Häusler, B. Kramer, *Phys. Rev. B Condens. Matter* **47**, 16353–16357 (1993).
17. G. W. Bryant, *Phys. Rev. Lett.* **59**, 1140–1143 (1987).
18. S. A. Mikhailov, *Phys. Rev. B Condens. Matter* **65**, 115312 (2002).
19. R. Egger, W. Häusler, C. Mak, H. Grabert, *Phys. Rev. Lett.* **82**, 3320–3323 (1999).
20. A. V. Filinov, M. Bonitz, Y. E. Lozovik, *Phys. Rev. Lett.* **86**, 3851–3854 (2001).
21. C. Yannouleas, U. Landman, *Phys. Rev. Lett.* **82**, 5325–5328 (1999).
22. A. Ghosal, A. Güçlü, C. Umrigar, D. Ullmo, H. U. Baranger, *Nat. Phys.* **2**, 336–340 (2006).
23. B. Szafran, F. Peeters, S. Bednarek, J. Adamowski, *Phys. Rev. B Condens. Matter Mater. Phys.* **69**, 125344 (2004).
24. A. Harju, S. Siljamäki, R. M. Nieminen, *Phys. Rev. B Condens. Matter* **65**, 075309 (2002).
25. Y. Li, C. Yannouleas, U. Landman, *Phys. Rev. B Condens. Matter Mater. Phys.* **76**, 245310 (2007).
26. H. E. Ercan, S. Coppersmith, M. Friesen, *Phys. Rev. B* **104**, 235302 (2021).
27. J. Corrigan *et al.*, *Phys. Rev. Lett.* **127**, 127701 (2021).
28. A. Mintairov *et al.*, *Phys. Rev. B* **97**, 195443 (2018).
29. S. Kalliakos *et al.*, *Nat. Phys.* **4**, 467–471 (2008).
30. C. Ellenberger *et al.*, *Phys. Rev. Lett.* **96**, 126806 (2006).
31. T. Ihn *et al.*, *Int. J. Mod. Phys. B* **21**, 1316–1325 (2007).
32. W. Jang *et al.*, *Nano Lett.* **21**, 4999–5005 (2021).
33. W. Jang *et al.*, *Nat. Commun.* **14**, 2948 (2023).
34. S. Pecker *et al.*, *Nat. Phys.* **9**, 576–581 (2013).
35. I. Shapir *et al.*, *Science* **364**, 870–875 (2019).
36. H. Li *et al.*, *Nat. Mater.* **20**, 945–950 (2021).
37. H. Li *et al.*, *Nat. Phys.* **17**, 1114–1119 (2021).
38. H. Li *et al.*, *Nat. Mater.* **23**, 633–638 (2024).
39. H. Li *et al.*, *Nat. Nanotechnol.* **19**, 618–623 (2024).
40. See additional text and data in supplementary materials.
41. F. Wu, T. Lovorn, E. Tutuc, A. H. MacDonald, *Phys. Rev. Lett.* **121**, 026402 (2018).
42. M. Angeli, A. H. MacDonald, *Proc. Natl. Acad. Sci. U.S.A.* **118**, e2021826118 (2021).
43. M. H. Naik, M. Jain, *Phys. Rev. Lett.* **121**, 266401 (2018).
44. H. Li, "Replication Data for: Wigner Molecular Crystals from Multi-electron Moiré Artificial Atoms," Harvard Dataverse, V1 (2024); https://doi.org/10.7910/DVN/QHJCBQ.

ACKNOWLEDGMENTS

Funding: This work was primarily funded by the US Department of Energy, Office of Science, Basic Energy Sciences, Materials Sciences and Engineering Division, under contract no. DE-AC02-05-CH11231 within the van der Waals heterostructure program KCFW16 (device fabrication, STM spectroscopy). Support was also provided by National Science Foundation award DMR-2221750 (surface preparation). S.T. acknowledges primary support from US Department of Energy-SC0020653 (materials synthesis), NSF CMMI1825594 (nuclear magnetic resonance and

transmission electron microscopy studies on crystals), NSF DMR-1955889 (magnetic measurements on crystals), NSF ECCS2052527 (for bulk electrical tests), DMR 2111812, and CMMI 2129412 (for optical tests on bulk crystals). K.W. and T.T. acknowledge support from the JSPS KAKENHI (grant nos. 21H05233 and 23H02052) and World Premier International Research Center Initiative (WPI), MEXT, Japan. The work at Massachusetts Institute of Technology was supported by the Air Force Office of Scientific Research (AFOSR) under award FA9550-22-1-0432. **Author contributions:** H.L., M.F.C., and F.W. conceived the project. H.L. and Z.X. fabricated the heterostructure device. H.L. and Z.X. performed the STM/STS (scanning tunneling spectroscopy) measurement, H.L., Z.X., A.Z., M.F.C., and F.W. discussed the experimental design and analyzed the experimental data. A.P.R., T.D., and L.F. performed the theoretical calculations. R.S., R.B., and S.T. grew the WS_2 crystals. K.W. and T.T. grew the hBN single crystal. All authors discussed the results and wrote the manuscript. **Competing interests:** The authors declare that they have no competing interests. **Data and materials availability:** All data shown in the main text and supplementary materials are available in the Harvard Dataverse (*44*).

SUPPLEMENTARY MATERIALS

science.org/doi/10.1126/science.adk1348
Materials and Methods
Supplementary Text
Figs. S1 to S5
References (*45*, *46*)
Movies S1 and S2

Submitted 4 August 2023; accepted 22 May 2024
10.1126/science.adk1348